





# Polarization-Sensitive Module for Optical Coherence Tomography Instruments

Po-Yi Lee, Chuan-Bor Chueh, Milen Shishkov, Tai-Ang Wang, Teresa Chen, Brett E. Bouma, and Martin Villiger

Abstract—Polarization-sensitive optical coherence tomography (PS-OCT) extends OCT by analyzing the polarization states of backscattered light to quantify tissue birefringence. However, conventional implementations require polarization-diverse detection and are therefore incompatible with most commercial OCT systems. As a result, PS-OCT has largely remained restricted to specialized research groups, limiting its broader scientific and clinical use. Here, we present a modular PS-OCT framework that integrates with a standard spectral-domain OCT platform through a detachable rotating achromatic half-wave plate in the sample arm. This waveplate modulates both incident and reflected polarization states. Three or more repeated measurements at distinct waveplate orientations enable reconstruction of the sample's round-trip Jones matrix and the corresponding polarization properties. To mitigate random phase variations between repeated measurements, we introduce a retarder-constrained phase optimization strategy. We validate the framework with imaging of birefringent phantoms and human retina in vivo, demonstrating reliable reconstruction of retardance and optic axis orientation. This approach requires only minimal hardware modification and is readily deployable on mainstream OCT systems. Lowering technical barriers paves the way for rapid and widespread deployment of PS-OCT across diverse biomedical applications in both research and clinical environments.

Index Terms—birefringence, retardance, Jones matrix, optic axis orientation, polarization-sensitive optical coherence tomography, retina.

# I. INTRODUCTION

Optical coherence tomography (OCT) is a non-invasive imaging technique that generates cross-sectional images of biological tissues at micrometer resolution. Since its introduction in 1991 [1], OCT has become an indispensable tool in biomedical imaging, with applications ranging from ophthalmology [2, 3] to cardiology [4, 5], gastrointestinal [6] and pulmonary [7] imaging, and dermatology [8]. Polarization-

sensitive OCT (PS-OCT) extends OCT by analyzing the polarization states of backscattered light, enabling tomographic reconstruction of tissue polarization properties such as birefringence and optic axis orientation [9, 10]. These polarimetric measurements offer insights into tissue microstructure beyond conventional OCT resolution, revealing information about tissue integrity, composition, and biomechanical factors. PS-OCT has been used to investigate a variety of tissues, including skin and its burns and scars [11-13], coronary arteries [14, 15], pulmonary airways [16, 17], and ocular tissues in studies of glaucoma [18, 19], age-related macular degeneration [20], and myopia [21, 22]. Despite these advances, PS-OCT has remained largely confined to research settings. Current implementations rely on custom-built systems with multiple polarization states for illumination and/or polarization-diverse detection channels [10]. The conventional PS-OCT frameworks are fundamentally incompatible with the widely deployed OCT platforms used in clinical and translational research. This incompatibility has hindered the development of commercially viable, clinically adaptable PS-OCT solutions, slowing progress across multiple fields of medicine. To enable broad adoption, PS-OCT requires a technical transition paradigm that integrates seamlessly with existing OCT systems while providing advanced polarization contrast. In this study, we introduce RevoPol, a novel PS-OCT framework that enables commercial spectral-domain OCT instruments to perform seamless polarimetric measurements through modular hardware modifications. By expanding PS-OCT capabilities to standard OCT platforms, RevoPol facilitates rapid deployment across diverse biomedical applications, from ophthalmology to other tissue imaging domains, accelerating both research and clinical translation.

# II. METHODS

# A. Imaging Framework and Setup

The novel PS-OCT framework, RevoPol, relies on inserting a rotating waveplate into the sample arm of a spectral-domain

This work will be submitted to the IEEE for possible publication. This work was supported in part by the U.S. National Institute of Health under Grants R01EB033321 and P41EB015903 and by Heidelberg Engineering. (*Corresponding author*: Po-Yi Lee)

This work involved human subjects in its research. Approval of all ethical and experimental procedures and protocols was granted by the Mass General Brigham Institutional Review Board.

Po-Yi Lee, Milen Shishkov, and Martin Villiger are with Wellman Center for Photomedicine, Massachusetts General Hospital, Somerville, MA 02145 (email: plee26@mgh.harvard.edu; mshishkov@mgh.harvard.edu; mvilliger@mgh.harvard.edu).

Brett E. Bouma is with Wellman Center for Photomedicine, Massachusetts General Hospital, Somerville, MA 02145 and also with Institute for Medical Engineering and Science, Massachusetts Institute of Technology, Cambridge, MA 02139 (email: bouma@mgh.harvard.edu)

Chuan-Bor Chueh and Tai-Ang Wang were with Wellman Center for Photomedicine, Massachusetts General Hospital, Somerville, MA 02145 Both are now with Graduate Institute of Photonics and Optoelectronics, National Taiwan University, Taipei, Taiwan 10617 (email: f06941077@ntu.edu.tw; d10941014@ntu.edu.tw)

Teresa Chen is with Department of Ophthalmology, Massachusetts Eye and Ear, Boston, MA 02114 (email: Teresa Chen@meei.harvard.edu).

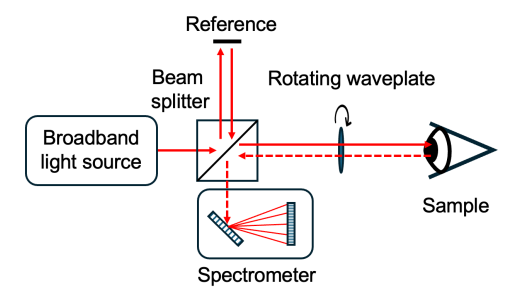


Fig. 1. Schematic of the RevoPol framework. A rotating waveplate, placed in the sample arm, modulates the polarization state of the probing light and enables extraction of tissue polarization properties on a standard spectral-domain OCT platform.

OCT instrument (Fig. 1). Specifically, employing an achromatic half-wave plate preserves the linearity of the source polarization state upon transmission while rotating it by twice the angle between the incident state and the waveplate's fast axis. During repeated cross-sectional imaging, the changing waveplate orientation modulates the polarization state of the illuminating and backscattered light to and from the sample. Every OCT system is natively sensitive to polarization due to its coherent measurement scheme. Only the portion of the backscattered light that matches the polarization of the reference light contributes to the interference signal. In the RevoPol framework, scatterers in non-birefringent tissues keep identical interference signals for all waveplate orientations, while the interference signals change in birefringent tissues dependent on waveplate orientations. This framework captures a sequence of at least three repeated cross-sectional images at the same location through the revolving waveplate, enabling reconstruction of the tissue's polarization properties.

To implement the rotating waveplate function in the RevoPol framework, we developed a module consisting of an achromatic half-wave plate (Edmund Optics, USA) driven by a beltcoupled DC motor, with rotation speed controlled by a motor controller (Fig. 2A). The module was tailored for integration with the Spectralis HRA+OCT instrument (Heidelberg Engineering, Germany) by insertion into the free-space section of the sample arm (Fig. 2B). The Spectralis combines a spectrometer-based OCT system—operating at 85 kHz A-line rate with a source centered on 870 nm—with a confocal scanning laser ophthalmoscope (SLO) providing a 30° field-ofview and 30-Hz active eye tracking. Simultaneous SLO imaging enables real-time eye motion tracking, which stabilizes OCT imaging by dynamically correcting scan locations. This capability also supports OCT angiography (OCTA) acquisition, which uses repeated scans at each sampling location. Leveraging this OCTA mode, RevoPol reconstructs tissue polarization properties by acquiring at least three repeated cross-sectional images at the same location, each corresponding to a different waveplate orientation. The Spectralis evaluates the quality of each set of repeated measurements immediately after acquisition. If a set fails to meet quality control—for example, due to motion artifacts or signal dropout—it is discarded and reacquired. With authorized software access from Heidelberg Engineering, raw OCT fringe data and B-scan timestamps can be exported for offline analysis. The associated

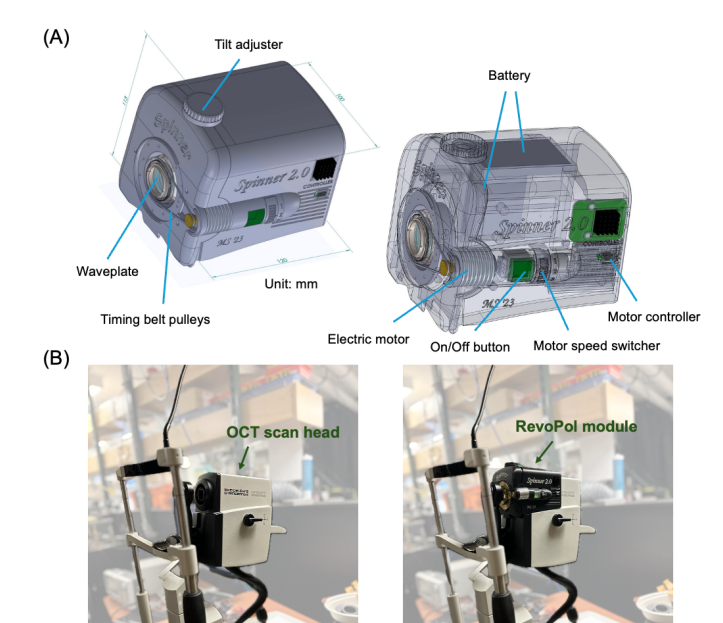


Fig 2. RevoPol module for the Spectralis HRA+OCT instrument. (A) The module consists of an achromatic half-wave plate driven by a belt-coupled DC motor. A motor controller, programmed via a micro-USB connection, allows the user to select rotation speeds using a dial on the module. The unit is powered by rechargeable batteries that can be recharged, eliminating the need for a wall outlet. The module operates independently and does not require synchronization with the OCT instrument. The tilt adjuster lowers the internal reflection from the waveplate. (B) A physical gap between the scan head and the objective lens facilitates integration of the module, which can be easily attached to and detached from the scan head.

signal formalism and processing workflow are described in the following sections.

# B. Terminology

**A-line:** A depth-resolved signal profile at a single lateral position.

**B-scan**: A cross-sectional image acquired by sequentially acquiring A-lines while scanning laterally along the fast axis.

**Repeated measurements**: Multiple acquisitions at the same B-scan position, typically performed in OCTA mode while the waveplate rotates. A set of repeated measurements is used to reconstruct a polarization-resolved cross-sectional image.

**C-scan**: A three-dimensional dataset formed by acquiring multiple sets of repeated measurements along the slow axis. The index of the reconstructed cross-sectional images is denoted as the slow-axis number (slow-axis #).

**Surface retardance**: The cumulative retardance measured at the sample surface, introduced by birefringent tissues along the imaging path (e.g., cornea in retinal imaging).

# C. Jones Matrix Reconstruction

The RevoPol framework performs repeated measurements through a rotating waveplate placed in the sample arm, each using a single input and detection state. Measurements through distinct waveplate orientations effectively correspond to different polarization states incident on the sample, and the collected back-scattered light interferes with the reference light.

Only the portion of the scattered light matching the polarization of the reference contributes to the interference signal, serving as a form of polarization detection. Algebraically, the recovered complex-valued tomogram can be expressed as

$$m(z,n) = \underbrace{\mathbf{f}^{\dagger} \cdot \mathbf{Q}^{\mathrm{T}}(\alpha + n\Delta\alpha)}_{\mathbf{f}_{\prime}n^{\dagger}} \cdot \mathbf{J}_{\mathcal{S}}(z) \cdot \underbrace{\mathbf{Q}(\alpha + n\Delta\alpha) \cdot \mathbf{e}}_{\mathbf{e}_{\prime}n}, \tag{1}$$

where  $\mathbf{Q}(\alpha + n\Delta\alpha)$  describes the transmission through the rotating half-wave plate at an initial angle  $\alpha$  increasing by  $\Delta\alpha$  between the sequential measurements, indexed by n.  $\mathbf{e}$  is the Jones vector of the source polarization state, and  $\mathbf{f}$  is the corresponding reference state.  $\mathbf{e'}_n$  and  $\mathbf{f'}_n$  denote the polarization states of the illumination and reference beams, respectively, after (reverse) transmission through the waveplate at the  $n^{\text{th}}$  measurements.  $\mathbf{J}_S(z)$  represents the  $2\times2$  round-trip Jones matrix of the tissue at depth z. Without loss of generality, the OCT system's free-space interferometer is linearly polarized and identical to the source polarization state (i.e.,  $\mathbf{e} = \mathbf{f}$ ).

Invoking the Kronecker product rule, each individual tomogram can be described as a linear projection of the unknown, vectorized Jones matrix  $\vec{J}_s(z)$  onto the known  $4\times1$  sensing vector  $\vec{g}_n$ , such that

$$m(z,n) = \underbrace{\mathbf{e'}_{n}^{\mathsf{T}} \otimes \mathbf{f'}_{n}^{\mathsf{+}}}_{\mathbf{g}_{n}} \cdot \overrightarrow{\mathbf{J}}_{S}(z). \tag{2}$$

Here, the sensing vector  $\mathbf{g}_n$  encodes the illumination and detection polarization states at a specific waveplate orientation.

A sequence of tomographic measurements **m** forms a linear system that relates the unknown, vectorized Jones matrix  $\overrightarrow{J_s}(z)$  to the known sensing matrix **G**:

It is important to note that when the sensing matrix is constructed using only a rotating waveplate with fixed retardance, its maximum column rank is three, regardless of the number of waveplate orientations. The intrinsic round-trip symmetry of OCT further imposes that  $\mathbf{J}_S(z) = \mathbf{J}_S^T(z)$ , and accordingly  $j_{21} = j_{12}$  [23, 24]. Thus, instead of four independent elements, each vectorized Jones matrix reduces to three independent complex-valued scalars. This reduction can be expressed using a modified sensing matrix  $\mathbf{G}'$  with only three columns:

$$\mathbf{m}(z) = \mathbf{G} \cdot \begin{bmatrix} j_{11}(z) \\ j_{21}(z) \\ j_{12}(z) \\ j_{22}(z) \end{bmatrix} = \underbrace{\mathbf{G} \cdot \begin{bmatrix} 100 \\ 010 \\ 001 \\ 001 \end{bmatrix}}_{\mathbf{G}'} \cdot \underbrace{\begin{bmatrix} j_{11}(z) \\ j_{21}(z) \\ j_{22}(z) \end{bmatrix}}_{\mathbf{J}'_{\mathcal{G}}(z)} = \mathbf{G}' \cdot \overline{\mathbf{J}'_{\mathcal{S}}}(z). \tag{4}$$

When the column rank of the modified sensing matrix is three—i.e., when  $\mathbf{G}'^{\dagger} \cdot \mathbf{G}'$  is invertible—the vectorized Jones matrix of the sample can be calculated using the pseudoinverse as

$$\overrightarrow{\mathbf{J}'_{S}}(z) = \left(\mathbf{G}'^{\dagger} \cdot \mathbf{G}'\right)^{-1} \cdot \mathbf{G}'^{\dagger} \cdot \mathbf{m}(z). \tag{5}$$

To achieve this condition, at least three tomographic measurements acquired with different waveplate orientations are required to enable unambiguous reconstruction of the sample's Jones matrix.

#### D. Phase Correction

Pathlength drift between the sample and reference arms introduces phase variations between repeated measurements of the complex-valued tomograms [25]. Our strategy for estimating these phase shifts is to perform phase optimization by minimizing the disagreement among repeated measurements obtained from more than three waveplate orientations.

Each acquired A-line measurement deviates from the ideal signal by an unknown, depth-independent phase shift combined with random noise. This effect can be modeled as

$$\widetilde{\mathbf{m}} = \operatorname{diag}(e^{-i\phi}) \cdot \mathbf{m} + \mathbf{\eta} = \operatorname{diag}(\overline{\Phi}) \cdot \mathbf{m} + \mathbf{\eta}, \tag{7}$$

where  $\varphi$  is a vector of unknown phase offsets (one per A-line measurement), and  $\eta$  is a noise matrix that perturbs the ideal measurements. Without loss of generality, the first element of  $\varphi$  is set to zero to define the global phase reference.

First, we compensate for phase differences  $\tilde{\phi}$  at the sample surface across repeated A-line measurements

$$\widetilde{\mathbf{m}}_0 = \operatorname{diag}(e^{i\widetilde{\boldsymbol{\varphi}}}) \cdot \widetilde{\mathbf{m}}. \tag{8}$$

We refer to this procedure as zero-phase correction, which eliminates random phase noise but also the meaningful phase offsets arising from tissue retardance along the light path, such as the cornea in retinal imaging.

Second, we recover this retarder-induced, meaningful phase offsets through optimization. We refer to this procedure as retarder-constrained phase optimization. From Eqs. (5) and (8), the sample's Jones matrix can be recovered as

$$\widehat{\overline{\mathbf{J}'_S}} = \left(\mathbf{G'}^{\dagger} \cdot \mathbf{G'}\right)^{-1} \cdot \mathbf{G'}^{\dagger} \cdot \operatorname{diag}(\mathbf{\Phi}_0) \cdot \widetilde{\mathbf{m}}_0, \tag{9}$$

where  $\Phi_0$  represents an estimate of the phase offsets arising from tissue birefringence along the light path. Any phase estimation vector results in a plausible Jones matrix. The most suitable phase compensation is obtained by minimizing the reconstruction error of the corresponding Jones matrix

$$\widehat{\mathbf{\Phi}} = \arg\min_{\mathbf{\Phi}_0} \left\| \operatorname{diag}(\mathbf{\Phi}_0) \cdot \widetilde{\mathbf{m}}_0 - \mathbf{G}' \cdot \widehat{\overline{\mathbf{J}'}_S} \right\|_2^2. \tag{10}$$

This phase estimation can be further simplified as

$$\begin{split} \widehat{\mathbf{\Phi}} &= \arg\min_{\mathbf{\Phi}_0} \|\mathbf{U} \cdot \operatorname{diag}(\mathbf{\Phi}_0) \cdot \widetilde{\mathbf{m}}_0\|_2^2 \\ &= \arg\min_{\mathbf{\Phi}_0} {\mathbf{\Phi}_0}^{\dagger} \cdot \mathbf{W} \cdot \mathbf{\Phi}_0, \end{split} \tag{11}$$

where  $\mathbf{U} = \mathbf{I} - \mathbf{G}' \cdot \left(\mathbf{G}'^\dagger \cdot \mathbf{G}'\right)^{-1} \cdot \mathbf{G}'^\dagger$  and  $\mathbf{W} = \operatorname{diag}(\widetilde{\mathbf{m}}_0)^\dagger \cdot \mathbf{U}^\dagger \cdot \mathbf{U} \cdot \mathbf{U}$  diag $(\widetilde{\mathbf{m}}_0)$ . The matrix  $\mathbf{W}$  is determined jointly by the tomographic measurements and the waveplate orientations, owing to  $\operatorname{diag}(\mathbf{\Phi}_0) \cdot \widetilde{\mathbf{m}}_0 = \operatorname{diag}(\widetilde{\mathbf{m}}_0) \cdot \mathbf{\Phi}_0$ . Because  $\mathbf{W}$  is noncoherent, it can be averaged along depth or across multiple Alines.

To further constrain the solution,  $\Phi_0$  is modeled as a linear retarder at the sample surface, denoted  $\mathbf{J}_{\mathrm{surf}}(\delta, \theta)$ , where  $\delta$  and  $\theta$  represent the retardance and optic axis orientation, respectively.

$$\mathbf{\Phi}_{0} = e^{i\angle(\mathbf{G}\cdot\mathbf{J}_{\mathbf{surf}}(\delta,\theta))}.$$
 (12)

This restriction ensures that the estimated phase offsets correspond to a physically plausible transformation.

Empirically, the optimization exhibits two local minima corresponding to similar retardance values, but optic axis orientations separated by  $\pi$ . To resolve this ambiguity, we enforce optic axis consistency across neighboring A-lines and B-scans and select the solution by comparing the residual errors at the minima. The chosen axis orientation then determines the corresponding phase offsets used for correction.

# E. Coherency Filtering

Coherency filtering aims to retain the spatial coherence properties of the OCT signal while suppressing noise and incoherent artifacts. A stack of RevoPol measurements acquired at different waveplate orientations at each pixel can be described as a complex vector **m**. The local coherency matrix is computed as the outer product

$$\mathbf{H} = \mathbf{m}\mathbf{m}^{\dagger},\tag{14}$$

which is a rank-1 Hermitian matrix. To suppress uncorrelated noise, the coherency matrices are spatially filtered, where the matrix  $\mathbf{H}_{\text{filt}}$  does not remain rank-1. The filtered coherency matrix is then decomposed by singular value decomposition,

$$\mathbf{H}_{\text{filt}} = \mathbf{V}\mathbf{S}\mathbf{V}^{\dagger}.\tag{15}$$

Only the dominant coherent mode is retained, and a denoised measurement vector is reconstructed as

$$\mathbf{m}_{\text{filt}} = \sqrt{\mathbf{s}_1} \mathbf{v}_1. \tag{16}$$

where  $\mathbf{v}_1$  is the leading singular vector and  $\mathbf{s}_1$  is its singular value, which encodes the coherent signal power. This corresponds to the least squares approximation of  $\mathbf{H}_{\text{filt}}$  with a rank-1 matrix.

We define a metric as the normalized ratio of the dominant singular value to the total energy,

$$Q = \frac{\mathbf{s}_1}{\sum_i \mathbf{s}_i},\tag{17}$$

which delineates tissue signal with a high Q from noise-dominated or dynamically changing areas featuring a low Q. Thresholds applied to this metric enable surface segmentation and filter out shadowing from blood vessels (e.g., large retinal vessels).

# F. Imaging Workflow

This study involved simulations, imaging of birefringence phantoms, and retinal imaging in healthy human eyes. Simulations were conducted to validate the RevoPol framework, while phantom experiments were used to calibrate the waveplate's rotation speed and confirm ex vivo robustness. The phantoms were fabricated from polycarbonate embedded in an epoxy matrix, as previously described [26], and an additional, static waveplate was inserted into the imaging path to simulate corneal birefringence. To demonstrate in vivo applicability, retinal imaging was performed in a healthy volunteer. The pilot human study adhered to the tenets of the Declaration of Helsinki and was approved by the Mass General Brigham Institutional Review Board (IRB). Written informed consent was obtained from all participants prior to enrollment. The following section details the procedures used to extract tissue polarization properties with the RevoPol framework.

Step 1: Image acquisition. The waveplate rotation speed was set to approximately  $\pi/12$  radians between each repeated B-scan. For a B-scan pattern comprising 1024 A-lines (20° field-ofview) at an A-line rate of 85 kHz, this corresponded to a rotation speed of approximately 3 revolutions per second. The actual rotation speed was calibrated by imaging a birefringent phantom and analyzing the periodicity of the resulting signal together with the uniformity of reconstructed optic axis orientation. While the waveplate was rotating, six tomograms were acquired at the same location using the system's OCTA mode to enable reconstruction of the Jones matrices for a cross-sectional image.

Step 2: Image pre-processing. Image registration was performed to align repeated A-line measurements, reducing motion artifacts and ensuring signal consistency for accurate phase analysis. For axial registration, correlation signals were computed along laterally filtered A-lines using the chirped ztransform to obtain an oversampled correlation plot within a limited range. The correlation peak was identified and refined by fitting a third-order polynomial, weighted by the effective correlation values. The frame with the highest overall correlation was selected as the reference. For lateral registration, tomograms were divided into smaller, 50% overlapping windows, and the same procedure was applied to each subwindow. This yielded an interpolated, continuous lateral shift function. Correlation was performed only between directly adjacent scans, and the resulting shifts were summed to obtain the cumulative displacement. Coherency filtering, surface segmentation, and zero-phase correction were subsequently applied to the registered tomograms.

Step 3: Phase offset estimation. The W matrix from (11) was constructed by averaging signals along depth over several pixels, guided by surface segmentation. A retarder-constrained

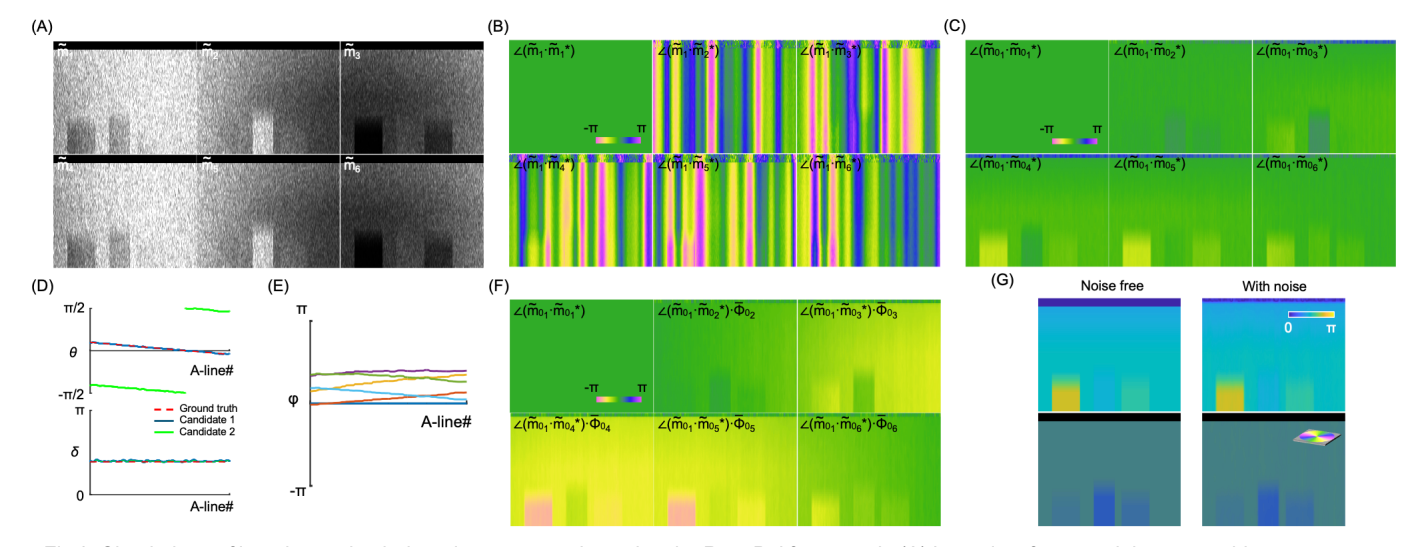


Fig 3. Simulations of imaging and polarimetric reconstruction using the RevoPol framework. (A) Intensity of sequential tomographic measurements acquired during waveplate rotation (rotation step:  $\pi/12$  per B-scan) with speckle and phase noise applied. Three birefringent bars and surface cumulative retardance were included in the simulation. (B) Phase differences between the first and subsequent measurements. (C) Phase differences after zero-phase correction. (D) Two candidate solutions of optic axis orientation ( $\theta$ ) and retardance ( $\delta$ ) obtained from retarder-constrained phase optimization, compared with the ground-truth retarder (red dashed line) The blue curve corresponds to the solution with smaller residual errors, while the green curve represents the rejected candidate. (E) Phase offsets ( $\phi$ ) generated from the estimated retarder corresponding to the blue curve in (D). (F) Final corrected phase differences obtained by applying the phase offsets from (E) to (C). (G) Cumulative retardance and optic axis orientation reconstructed from tomograms with corrected phases, compared with polarimetric reconstruction from noise-free signals.

phase optimization was then applied to estimate candidate optic axis orientations and retardance values. Each A-line yields two possible optic axis orientations; these were separated into two groups along the B-scan or C-scan. The group with the smaller overall residual error was selected, and the corresponding optic axis orientation and retardance were used to determine the phase offset. This step can be skipped if no birefringent material is present along the imaging path.

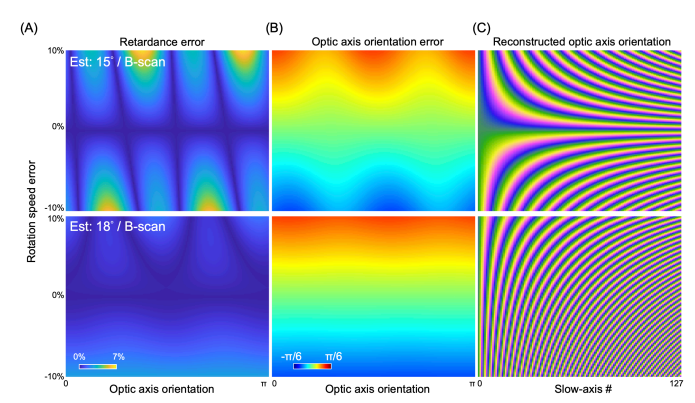
<u>Step 4: Polarimetric reconstruction.</u> The estimated phase offsets were applied to the filtered tomograms, followed by reconstruction of the complex-valued Jones matrix representing the polarization response of the sample. The Jones matrix was then decomposed into a unitary rotation matrix, from which the cumulative retardance and optic axis orientation were extracted. The optic axis orientations were compensated for the waveplate rotation, determined by the rotation speed, the inter-B-scan time interval, and the B-scan timestamps.

Step 5: Surface retardance compensation. Surface retardance, originating from birefringent tissues along the imaging path (e.g., the cornea [27]), was extracted as rotation vectors. The square root of these vectors was converted into Jones matrices and applied symmetrically to the measured Jones matrices, thereby removing the cumulative retardance contribution along the imaging path [21].

# III. RESULTS

#### A. Simulation

We used numerical simulations to assess the ability of the RevoPol framework to reconstruct polarization properties. The simulated dataset included speckle and phase noise, as well as known birefringent structures consisting of three embedded bars and significant cumulative surface retardance. Sequential tomographic measurements were generated during waveplate rotation, and phase differences were computed relative to the initial acquisition (**Fig. 3A–B**). With the waveplate increment of  $\pi/12$  radians between repeated B-scans, the first–fourth, second–fifth, and third–sixth measurements exhibited matching intensities but showed distinct phase differences. Zero-phase correction effectively removed random phase noise (**Fig. 3C**). Retarder-constrained phase optimization then produced two candidate solutions for optic axis orientation and retardance (**Fig. 3D**). Comparison with the ground-truth retarder confirmed that the solution with smaller residual errors was the correct one. Using this validated solution, we extracted the phase offsets (**Fig. 3E**). Applying the recovered phase offsets enables accurate reconstruction of cumulative retardance and



4. Simulation of rotation speed error on polarimetric reconstruction. Estimated rotation speeds (ω) are 15°/B-scan (top) and 18°/B-scan (bottom). Rotation speed error is defined  $(\omega_{actual} - \omega_{estimated})/\omega_{estimated} \times 100\%$ . (A) Retardance error and (B) optic axis orientation error as a function of known optic axis orientation. (C) Reconstruction of a constant optic axis orientation along the B-scan direction without compensation for continuous rotation. With an estimated speed of 15°/B-scan, the orientation remains constant when the rotation speed is correct (Rotation speed error = 0%) and exhibits progressive variation in the presence of speed error. In contrast, an estimated speed of 18°/B-scan produces high-frequency fluctuations in the reconstructed orientations, regardless of speed accuracy.

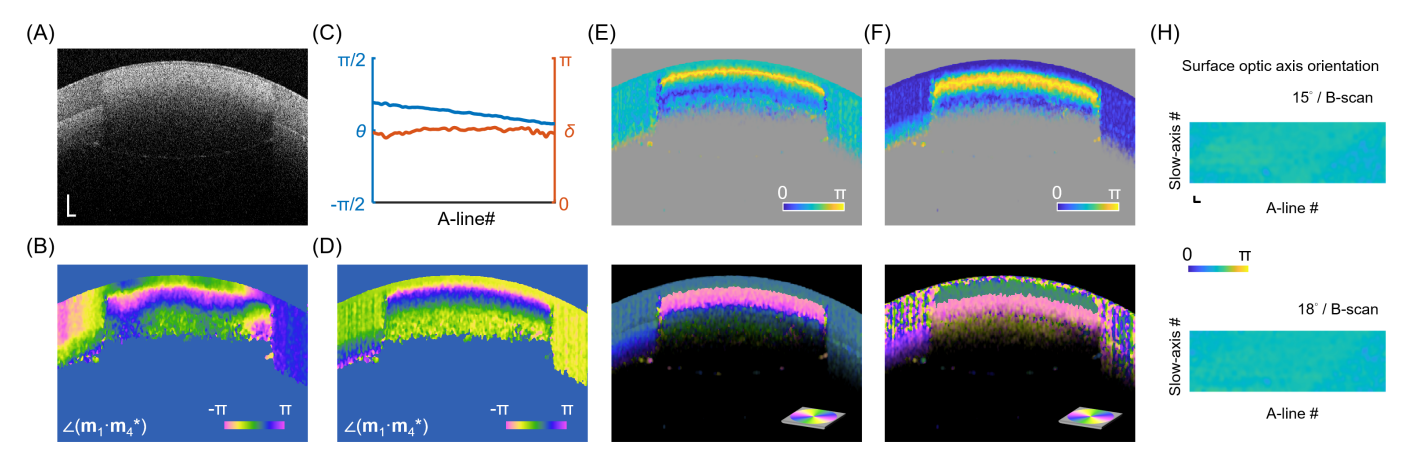


Fig 5. Imaging of a birefringence phantom using the RevoPol framework. (A) Structural B-scan. (B) Phase difference map before correction. (C) Optic axis orientation ( $\theta$ ) and retardance ( $\delta$ ) estimated using retarder-constrained phase optimization. (D) Phase difference map after correction. (E) Cumulative retardance and optic axis orientation reconstructed from corrected tomograms. (F) Cumulative retardance and optic axis orientation after surface retardance compensation. (H) Surface retardance maps acquired using different waveplate rotation speeds. All scale bars: 200  $\mu$ m.

optic axis orientation (**Fig. 3F–G**). We evaluated the effect of rotation speed estimation on polarimetric reconstruction. We found that an estimated speed of  $18^{\circ}$  ( $\pi/10$ ) per B-scan was the most robust against errors in reconstructed retardance and optic axis orientation (**Fig. 4A–B**). In comparison, at  $15^{\circ}$  ( $\pi/12$ ) per B-scan the reconstructed orientation remained largely stable along slow-axis scan, showing only minor drifts in a C-scan under estimation error when continuous rotation was not compensated (**Fig. 4C**).

# B. Phantom Imaging

We applied the RevoPol framework to a birefringent phantom with a retarder placed in the imaging path to experimentally validate the reconstruction workflow, using a waveplate rotation speed of  $\pi/12~(\sim15^\circ)$  per B-scan (Fig. 5A-F). Phase shifts were uniform along each A-line but varied randomly between successive A-lines (Fig. 5B). Using retarder-constrained phase optimization, we obtained optic axis orientation and retardance at the surface, where the apparent optic axis orientation varied with waveplate rotation while the retardance remained constant (Fig. 5C). Using the correct solution, consistent phase offsets were recovered, which enabled reconstruction of cumulative retardance and optic axis

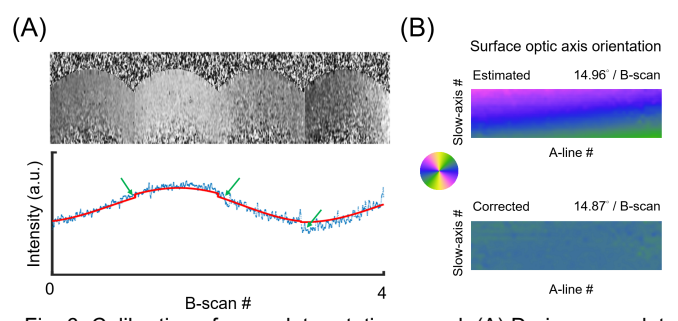


Fig. 6. Calibration of waveplate rotation speed. (A) During waveplate rotation, the fixed retarder placed along the light path induced periodic intensity modulation in the phantom. After coherence filtering, the normalized intensity across repeated B-scans (blue) shows a periodicity of 3 B-scans, corresponding to a waveplate rotation speed of  $\pi/12$  (~15°) per B-scan. The intensity inconsistency between B-scans (green arrows) indicates inter-B-scan time. (B) In a C-scan, the reconstructed surface optic axis orientation shows drifts (top) due to small deviations in the estimated rotation speed. Precise calibration of the waveplate rotation speed eliminates these drifts (bottom).

orientation across the phantom (Fig. 5D–E). Polarization properties were further corrected through surface retardance compensation, ensuring that the reconstructed properties originated from the phantom itself (Fig. 5F). We measured cumulative retardance at the surface using different waveplate rotation speeds (Fig. 5H). Both measurements exhibited consistent patterns, demonstrating that the polarimetric reconstruction was independent of the waveplate speed.

We used a non-birefringent phantom with a retarder placed in the imaging path to calibrate the waveplate rotation increment per B-scan (**Fig. 6**). For a rough estimation, we analyzed the signal intensity modulated by a fixed retarder along the imaging path (**Fig. 6A**). After applying coherence filtering, the normalized intensity across repeated B-scans exhibited a periodicity of three B-scans. The intensity varies as

$$I = |m|^2 \propto \cos(8\psi),\tag{18}$$

where  $\psi$  is half-waveplate fast-axis angle, i.e., the angular period of the waveplate is one-eighth of the observed intensity period. This yielded a waveplate rotation speed of  $\pi/12$  (~15°) per B-scan. For accurate calibration, the reconstructed surface optic axis orientations in a C-scan are highly sensitive to rotation speed (**Fig. 6B**), making uniform orientation across the scan a reliable metric for precise waveplate calibration.

#### C. Retinal Imaging

In retinal imaging, the original tomogram exhibited strong speckle fluctuations (**Fig. 7A**). After registration and coherency filtering, speckle noise was substantially suppressed while structural boundaries were preserved (**Fig. 7B**). The Q metric further highlights retinal boundaries and effectively excludes regions shadowed by blood flow (**Fig. 7C**). The corresponding phase-difference maps (**Fig. 7D**) show that the original data contain significant phase noise within A-lines. Registration reduces this noise, and coherency filtering further suppresses high-frequency fluctuations while retaining phase-difference features, i.e., the phase variations along each A-line. It is worth noting that these A-line phase fluctuations are more pronounced in retinal data than in phantom experiments, primarily due to

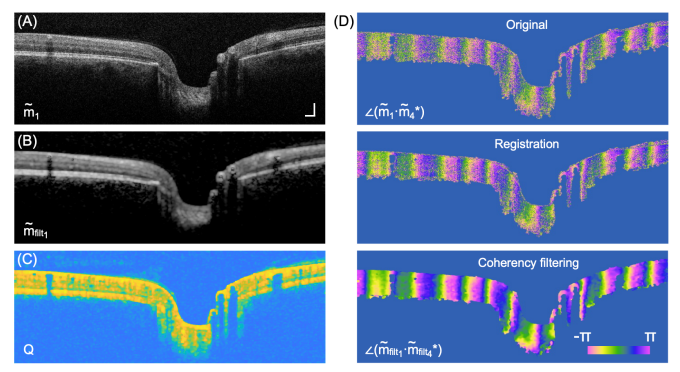


Fig. 7. Effect of coherency filtering on tomograms. (A) Original tomogram. (B) Tomogram after registration and coherency filtering, shown without phase correction. (C) Q metric derived from the coherency matrix, used to enhance boundary contrast. (D) Phase difference between the first tomogram and a repeated measurement for the original, registered, and coherency-filtered data, masked by Q > 0.4. Registration reduces phase noise, and coherency filtering further suppresses speckle and phase fluctuations while preserving structural boundaries. Scale bar: 200  $\mu m$ .

eye motion in vivo compared with the stationary phantom. Then, we demonstrated the feasibility of RevoPol reconstruction in healthy human retina (Fig. 8). At the ONH-centered scan, the surface retardance and optic axis orientation appeared spatially uniform (Fig. 8A), suggesting that corneal birefringence along the light path can be effectively modeled as a well-aligned retarder. After compensating for this surface contribution, the cumulative retardance exhibited a circumpapillary annular pattern consistent with birefringence distributions reported in previous studies using conventional PS-OCT. In the foveacentered scan (Fig. 8B) [28]. the Henle's fiber layer was clearly visualized, showing reduced retardance near the foveal center and the characteristic radial optic axis orientation of photoreceptor axons. These birefringence features are in close agreement with established findings [21, 29]. The clear visualization of retinal birefringence and organization highlights the ability of RevoPol to recover physiologically relevant polarization signatures in vivo with minimal hardware modification to the clinical OCT platform.

# IV. DISCUSSION

In this study, we presented RevoPol, a new PS-OCT framework that enables full Jones matrix reconstruction using a single-detector OCT system. As a practical implementation, we developed a detachable rotating waveplate module that can be integrated into a commercial OCT platform. Using this setup, we demonstrated reconstruction of retardance and optic axis orientation in both birefringent phantoms and the healthy human retina. These results confirm that RevoPol achieves effective reconstruction of known polarization signatures in vivo through a simple add-on module compatible with existing OCT hardware. Although demonstrated here with spectral-domain OCT, the RevoPol framework should be compatible with swept-source systems, as the optic axis shift of the waveplate within a single A-line is negligible.

Compared with existing PS-OCT methods, RevoPol offers distinct advantages. A previous study employed a linear polarizer followed by an LCD-based addressable wave plate set

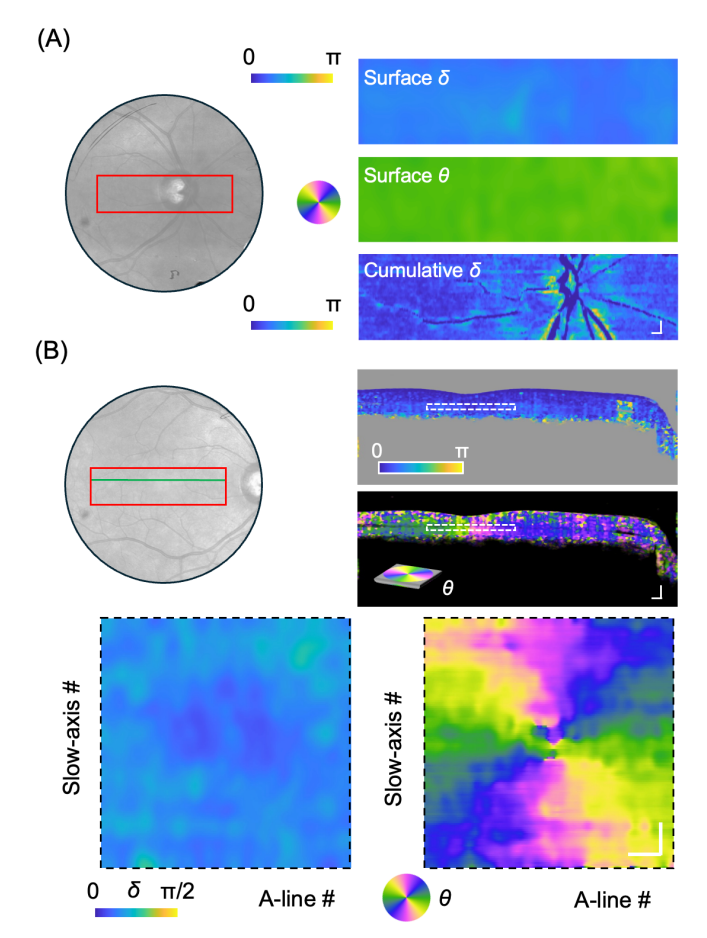


Fig. 8. Polarimetric reconstruction of healthy human retina using RevoPol (A) *Left*: Scanning laser ophthalmoscopy (SLO) image with the scan region centered on the ONH (red box). *Right*: En face, surface retardance ( $\delta$ , 48.5°±5.4°), surface optic axis orientation ( $\theta$ ), and cumulative retardance maps after surface retardance compensation, with vessel regions excluded. (B) *Left*: SLO image with the scan region centered on the fovea (red box). *Right*: B-scan cumulative retardance and optic axis orientation after surface retardance compensation corresponding to the green line in the SLO image. En face images of the Henle's fiber layer obtained from the white box in, showing reduced retardance and the characteristic radial optic axis orientation pattern. All scale bars: 200 µm.

to 45°, 90°, and 135° [30]. This configuration required longer imaging times and lacked phase correction, which prevented its use for in vivo imaging. Conventional PS-OCT with a single circular input state is limited to reporting cumulative retardance or assuming a uniform optic axis orientation with depth [31, 32]. This limitation arises from an intrinsic degeneracy in the polarization measurement: whenever the detected polarization state coincides with the mirror state of the input—that is, the same state with flipped helicity reflected across the horizontal QU-plane on the Poincaré sphere—the reconstruction becomes indeterminate [33, 34]. For example, with a perfectly circular input state and an observed circular state of opposite handedness, the measured retardance is  $\pi$ , yet the optic axis orientation cannot be determined. In contrast, RevoPol enables full Jones matrix reconstruction, allowing calculation of both depth-resolved birefringence and optic axis orientation. While multi-input PS-OCT offers robust polarimetric reconstruction, its implementation typically relies on depth-multiplexing [35, 36] or electro-optic polarization modulators [37] in

combination with polarization-diverse detection. These requirements substantially increase system complexity and have limited widespread translational and clinical adoption. In contrast, RevoPol employs sequential polarization modulation with a rotating waveplate, combined with a sensing matrix and retarder-constrained phase optimization, to recover tissue polarization properties using standard OCT hardware. This framework preserves the integrity of the underlying OCT system, and its modular design favors clinical translation, particularly in multi-site studies where standardization is critical. Note that the goal of RevoPol is not to replace conventional PS-OCT but to provide an accessible approach for polarimetric imaging in both clinical and research settings.

The choice of waveplate rotation speed plays an important role in the accuracy and practicality of RevoPol reconstruction. Ideally, any rotation speed would be sufficient for polarimetric reconstruction within the RevoPol framework. In practice, however, the selected speed affects reconstruction stability and quality control. From simulations with six repeated measurements, we found that a  $\pi/10$  rotation step provides the greatest robustness against reconstruction errors when the estimated speed deviates from the actual speed. For retinal imaging, however, we implemented six repeated measurements with a  $\pi/12$  rotation step. Under this configuration, the reconstructed optic axis orientations are expected to remain approximately constant along the slow-axis direction in a C-scan, which facilitates estimation of the actual rotation speed, particularly in cases where imaging timestamps are inaccurate or unavailable. In addition, the first-fourth, second-fifth, and third-sixth measurements should exhibit matching intensities because they correspond to orthogonal polarization states. This feature may provide a convenient quality-control metric for active eye-tracking. The current, unsynchronized setup simplifies implementation but introduces two limitations: (i) because only an averaged rotation speed is estimated, intravolume speed fluctuations may be missed, potentially introducing residual phase errors; and (ii) the initial optic axis orientation of the rotating waveplate is unknown, complicating cross-dataset comparisons, though retardance estimates remain unaffected.

Phase correction is critical for accurate polarimetric reconstruction in the RevoPol framework. Phase drift in OCT measurements follows an approximate 1/f behavior [25]. Variations are minimal over short timescales but can accumulate substantially over longer acquisitions. RevoPol acquires repeated B-scans over longer timescales (~10<sup>-2</sup> s), making the reconstruction more susceptible to phase drift and motion artifacts. When no birefringent material is present along the light path, zero-phase correction informed by the surface signal can be applied, uniformly resetting the phase across all A-lines. In retinal imaging, however, corneal birefringence introduces cumulative retardance at the sample surface, invalidating this simple approach. In such cases, phase offset estimation is required. Unconstrained phase optimization (Eq. 10) introduces unknown phase terms that grow with the number of repeated measurements, producing multiple local minima and ambiguity. By modeling the cornea as a pure retarder, the number of unknown parameters is reduced to two.

Retarder-constrained phase optimization, therefore, provides a robust strategy for estimating the phase offsets induced by the anterior segment. Moreover, this approach allows spatial filtering of the estimated retarder before conversion into phase offsets, suppressing local noise and discontinuities and thereby improving the stability of the reconstructed optic axis orientation. Since the cornea is considered a highly ordered birefringent tissue [38] and the surface retardance corresponds to a very small region, it is reasonable that we observed a uniform collagen structure with nearly constant retardance.

Both surface retardance compensation and accurate phase correction rely on reliable surface segmentation. In retinal imaging, however, surface detection is often challenged by speckle noise, low signal contrast at certain boundaries, and local signal dropout caused by vessels or eye motion [39]. Conventional segmentation methods frequently fail to provide smooth and continuous delineation under these conditions. which in turn compromises the stability of the reconstructed polarimetric parameters. These limitations are not unique to RevoPol. To address this, we developed a Q metric (Eq. 17) based on the ratio of the dominant singular value to the total energy of the coherency matrix. This metric, analogous to the degree of polarization, enhances surface contrast by suppressing speckle fluctuations while preserving structural boundaries, thereby improving the robustness of surface segmentation.

In summary, we demonstrated that RevoPol enables reliable reconstruction of retardance and optic axis orientation in both phantoms and human retina, requiring only minimal hardware modification to a commercial OCT platform. This framework extends the applicability of PS-OCT beyond retinal imaging and is suitable for both ex vivo and in vivo studies across diverse research and clinical settings. By lowering technical barriers, RevoPol facilitates broader adoption of polarization-sensitive OCT for diverse diagnostic, translational, and research applications.

# **ACKNOWLEDGMENT**

The authors gratefully acknowledge Prof. Hsiang-Chieh Lee for recommending his PhD students, Ting-Yen Tsai, Ting-Hao Chen, Tai-Ang Wang and Chuan-Bor Chueh, to participate in this project. The authors also acknowledge support from the Ministry of Science and Technology (Taiwan) through the Graduate Students Study Abroad Program, which enabled the participation of Chuan-Bor Chueh in this work.

# REFERENCES

- [1] D. Huang *et al.*, "Optical coherence tomography," *Science*, vol. 254, no. 5035, pp. 1178-1181, 1991.
- [2] W. Drexler and J. G. Fujimoto, "State-of-the-art retinal optical coherence tomography," *Progress in Retinal and Eye Research*, vol. 27, no. 1, pp. 45-88, 2008.
- [3] E. A. Swanson and J. G. Fujimoto, "The ecosystem that powered the translation of OCT from fundamental research to clinical and commercial impact," *Biomedical Optics Express*, vol. 8, no. 3, pp. 1638-1664, 2017.
- [4] G. J. Tearney et al., "Consensus standards for acquisition, measurement, and reporting of intravascular optical coherence tomography studies: a report from the International Working Group for Intravascular Optical Coherence Tomography Standardization

- and Validation," *Journal of the American College of Cardiology*, vol. 59, no. 12, pp. 1058-1072, 2012.
- [5] Z. Ali, K. K. Galougahi, G. S. Mintz, A. Maehara, R. Shlofmitz, and A. Mattesini, "Intracoronary optical coherence tomography: state of the art and future directions: State of the art in OCT," *EuroIntervention*, vol. 17, no. 2, p. e105, 2021.
- [6] T.-H. Tsai et al., "Optical coherence tomography in gastroenterology: a review and future outlook," Journal of Biomedical Optics, vol. 22, no. 12, pp. 121716-121716, 2017.
- [7] H. Pahlevaninezhad and S. Lam, "Optical Coherence Tomography: A Review," *Interventions in Pulmonary Medicine*, pp. 379-391, 2023.
- [8] B. Wan et al., "Applications and future directions for optical coherence tomography in dermatology," British Journal of Dermatology, vol. 184, no. 6, pp. 1014-1022, 2021.
- [9] M. R. Hee, D. Huang, E. A. Swanson, and J. G. Fujimoto, "Polarization-sensitive low-coherence reflectometer for birefringence characterization and ranging," *JOSA B*, vol. 9, no. 6, pp. 903-908, 1992.
- [10] J. F. De Boer, C. K. Hitzenberger, and Y. Yasuno, "Polarization sensitive optical coherence tomography—a review," *Biomedical Optics Express*, vol. 8, no. 3, pp. 1838-1873, 2017.
- [11] E. Li, S. Makita, Y.-J. Hong, D. Kasaragod, and Y. Yasuno, "Three-dimensional multi-contrast imaging of in vivo human skin by Jones matrix optical coherence tomography," *Biomedical Optics Express*, vol. 8, no. 3, pp. 1290-1305, 2017.
- [12] K. H. Kim *et al.*, "In vivo imaging of human burn injuries with polarization-sensitive optical coherence tomography," *Journal of Biomedical Optics*, vol. 17, no. 6, pp. 066012-066012, 2012.
- [13] W. C. Lo et al., "Longitudinal, 3D imaging of collagen remodeling in murine hypertrophic scars in vivo using polarization-sensitive optical frequency domain imaging," Journal of Investigative Dermatology, vol. 136, no. 1, pp. 84-92, 2016.
- [14] M. Villiger et al., "Coronary plaque microstructure and composition modify optical polarization: a new endogenous contrast mechanism for optical frequency domain imaging," *JACC: Cardiovascular Imaging*, vol. 11, no. 11, pp. 1666-1676, 2018.
- [15] K. Otsuka, M. Villiger, S. K. Nadkarni, and B. E. Bouma, "Intravascular polarimetry: clinical translation and future applications of catheter-based polarization sensitive optical frequency domain imaging," *Frontiers in Cardiovascular Medicine*, vol. 7, p. 146, 2020.
- [16] D. C. Adams et al., "Birefringence microscopy platform for assessing airway smooth muscle structure and function in vivo," Science Translational Medicine, vol. 8, no. 359, pp. 359ra131-359ra131, 2016.
- [17] S. Nandy et al., "Polarization-sensitive endobronchial optical coherence tomography for microscopic imaging of fibrosis in interstitial lung disease," American Journal of Respiratory and Critical Care Medicine, vol. 206, no. 7, pp. 905-910, 2022.
- [18] R. R. Parakkel et al., "Retinal nerve fiber layer damage assessment in glaucomatous eyes using retinal retardance measured by polarization-sensitive optical coherence tomography," Translational Vision Science & Technology, vol. 13, no. 5, pp. 9-9, 2024.
- [19] S. Steiner *et al.*, "Birefringent properties of the peripapillary retinal nerve fiber layer in healthy and glaucoma subjects analyzed by polarization-sensitive OCT," *Investigative Ophthalmology & Visual Science*, vol. 63, no. 12, pp. 8-8, 2022.
- [20] R. Terao et al., "Quantification of Hyperreflective Foci in Age-Related Macular Degeneration by Polarization Sensitive Optical Coherence Tomography," Ophthalmology Science, p. 100792, 2025.
- [21] X. Liu et al., "Posterior scleral birefringence measured by tripleinput polarization-sensitive imaging as a biomarker of myopia progression," *Nature Biomedical Engineering*, pp. 1-15, 2023.
- [22] K. Ohno-Matsui et al., "Polarization-sensitive OCT imaging of scleral abnormalities in eyes with high myopia and dome-shaped macula," JAMA Ophthalmology, vol. 142, no. 4, pp. 310-319, 2024.
- [23] M. Villiger, B. Braaf, N. Lippok, K. Otsuka, S. K. Nadkarni, and B. E. Bouma, "Optic axis mapping with catheter-based polarization-sensitive optical coherence tomography," *Optica*, vol. 5, no. 10, pp. 1329-1337, 2018.
- [24] N. Vansteenkiste, P. Vignolo, and A. Aspect, "Optical reversibility theorems for polarization: application to remote control of

- polarization," *Journal of the Optical Society of America A*, vol. 10, no. 10, pp. 2240-2245, 1993.
- [25] B. J. Vakoc, S.-H. Yun, J. d. Boer, G. J. Tearney, and B. E. Bouma, "Phase-resolved optical frequency domain imaging," *Optics Express*, vol. 13, no. 14, pp. 5483-5493, 2005.
- [26] X. Liu, K. Beaudette, X. Wang, L. Liu, B. E. Bouma, and M. Villiger, "Tissue-like phantoms for quantitative birefringence imaging," *Biomedical Optics Express*, vol. 8, no. 10, pp. 4454-4465, 2017.
- [27] M. Pircher, É. Götzinger, B. Baumann, and C. K. Hitzenberger, "Corneal birefringence compensation for polarization sensitive optical coherence tomography of the human retina," *Journal of Biomedical Optics*, vol. 12, no. 4, pp. 041210-041210-10, 2007.
- [28] E. Götzinger *et al.*, "Retinal pigment epithelium segmentation by polarization sensitive optical coherence tomography," *Optics Express*, vol. 16, no. 21, pp. 16410-16422, 2008.
- [29] M. Sugita et al., "Motion artifact and speckle noise reduction in polarization sensitive optical coherence tomography by retinal tracking," Biomedical Optics Express, vol. 5, no. 1, pp. 106-122, 2013.
- [30] J. E. Roth, J. A. Kozak, S. Yazdanfar, A. M. Rollins, and J. A. Izatt, "Simplified method for polarization-sensitive optical coherence tomography," *Optics Letters*, vol. 26, no. 14, pp. 1069-1071, 2001.
- [31] C. Fan and G. Yao, "Mapping local optical axis in birefringent samples using polarization-sensitive optical coherence tomography," *Journal of Biomedical Optics*, vol. 17, no. 11, pp. 110501-110501, 2012.
- [32] C. Fan and G. Yao, "Mapping local retardance in birefringent samples using polarization sensitive optical coherence tomography," *Optics Letters*, vol. 37, no. 9, pp. 1415-1417, 2012.
- [33] Q. Xiong *et al.*, "Constrained polarization evolution simplifies depth-resolved retardation measurements with polarization-sensitive optical coherence tomography," *Biomedical Optics Express*, vol. 10, no. 10, pp. 5207-5222, 2019.
- [34] G. L. Jones, Q. Xiong, X. Liu, B. E. Bouma, and M. Villiger, "Single-input polarization-sensitive optical coherence tomography through a catheter," *Biomedical Optics Express*, vol. 14, no. 9, pp. 4609-4626, 2023.
- [35] B. Baumann, W. Choi, B. Potsaid, D. Huang, J. S. Duker, and J. G. Fujimoto, "Swept source/Fourier domain polarization sensitive optical coherence tomography with a passive polarization delay unit," *Optics Express*, vol. 20, no. 9, pp. 10229-10241, 2012.
- [36] Y. Lim, Y.-J. Hong, L. Duan, M. Yamanari, and Y. Yasuno, "Passive component based multifunctional Jones matrix swept source optical coherence tomography for Doppler and polarization imaging," *Optics Letters*, vol. 37, no. 11, pp. 1958-1960, 2012.
- [37] B. H. Park et al., "Real-time fiber-based multi-functional spectral-domain optical coherence tomography at 1.3 mu m," Optics Express, vol. 13, no. 11, pp. 3931-3944, 2005.
- [38] K. M. Meek and C. Knupp, "Corneal structure and transparency," Progress in Retinal and Eye Research, vol. 49, pp. 1-16, 2015.
- [39] M. A. Mayer, J. Hornegger, C. Y. Mardin, and R. P. Tornow, "Retinal nerve fiber layer segmentation on FD-OCT scans of normal subjects and glaucoma patients," *Biomedical Optics Express*, vol. 1, no. 5, pp. 1358-1383, 2010.